Supporting information:

Analysis of the voltage losses in CZTSSe solar cells of varying Sn content

Mohammed Azzouzi,[1,#] Antonio Cabas Vidani,[2,#] Stefan Haass,[2] Jason Rohr,[1] Yaroslav E.Romanyuk,[2] Ayodhya N. Tiwari,[2] Jenny Nelson[1,*].

[1] Department of Physics and Centre for Plastic Electronics, Imperial College London, London SW7 2AZ, United Kingdom.

[2] Laboratory for Thin Films and Photovoltaics, Empa-Swiss Federal Laboratories for Materials Science and Technology, Ueberlandstr. 129, 8600 Duebendorf, Switzerland

[#] These authors contributed equally

[*] Corresponding Author: jenny.nelson@imperial.ac.uk

EXPERIMENTAL SECTION

Device preparation. The precursor solution consisted of thiourea (99%+, Sigma- Aldrich), tin chloride dihydrate ($SnCl_2 \cdot 2H_2O$, 98%, Sigma-Aldrich), zinc chloride ($ZnCl_2$, 99.99%, Alfa Aesar) and copper chloride dihydrate ($CuCl_2 \cdot 2H_2O$, ≥99.99%, Sigma-Aldrich), dissolved in dimethyl sulfoxide (DMSO, 99.9%, Alfa Aesar). A 200–300 nm thick SiOx alkali diffusion barrier layer was sputtered onto a 1 mm thick soda-lime glass with a subsequent deposition of 1 μm of molybdenum. The precursor solution was spin-coated onto the Mo layer and dried on a hotplate at 320 °C in air. The spin-coating and drying steps were repeated 12 times in order to obtain the desired precursor film thickness of 1.5 μm. All devices were annealed in a rapid thermal processing furnace (RTP Annealsys AS ONE 150) inside a closed graphite box with selenium pellets (800 mg). The temperature gradient employed for annealing was the three-stage process with holding at 300, 500, and 550 °C. After selenization the absorbers were immersed for 30 s in a 10 wt% KCN solution in order to remove any eventual copper-rich phases and clean the surface from contaminations and oxides. A 50–70 nm thick CdS buffer layer was deposited by chemical bath deposition, and 70 nm/250 nm i-ZnO/Al:ZnO bilayer was sputtered. A Ni/Al top grid and an antireflection coating of MgF_2 were deposited by e-beam evaporation. Individual solar cells were mechanically scribed to an area of 0.30 ± 0.02 cm².

The JV characterization was performed under standard test conditions (100 mW cm−2, 25 °C, AM1.5G solar spectrum) using a solar simulator calibrated with a certified Si diode. **XRD** patterns for thin films were recorded in 2θ/θ scan mode using a Bruker D8 diffractometer with CuKα radiation (λ = 1.5418 Å, beam voltage: 40 kV, beam current: 40 mA, calibrated using Si100 and Si111 single crystals), a step size of 0.05°, and a scan rate of 0.5 s step−1 for the full pattern and a step size of 0.005° and a scan rate of 2 s step−1 for the high resolution pattern. **C*f*T and JVT measurements** were carried out with an LCR meter from Agilent (E4990A) with an AC voltage of 30 mV in the temperature range from 123 to 323 K. An Rp-Cp model was used to fit the admittance data. Measurements were performed under zero bias voltage for temperatures ranging from 123K to 323K and frequency from 100Hz and 1MHz. It is know from CIGSe that light or voltage soaking can change the state of the device due to

metastabilities.[52,61] The device was therefore left in the dark at 300K over night (at least 10 h) prior to an admittance measurement in order to put the device into an equilibrium state. At low-T (up to 203K) the spectra converge at the highest frequency to a low capacitance value, namely the geometric capacitance of the cell (C_g). The converging frequency is denoted as inflection frequency f_t and the transition to C_g reflects the dielectric freeze-out. At high-T the capacitance transition fits a Gaussian broad deep defect distribution, as described elsewhere.[53] The inflection frequencies are obtained from measured capacitance spectra from the derivative of the capacitance: $C'(f) = f * \frac{dC}{df}$. An Arrhenius plot drawn with $\ln f_t T^{-2}$ versus 1/T results in a straight line where the slope represents the defect energy E_a (C_f-T). For **CV measurements** the voltage was forward swept from -1 to 0.5 V at a frequency of 1 kHz.

Electroluminescence (EL) and Photoluminescence (PL). The measurement was done using a Shamrock 303 spectrograph combined with an iDUS InGaAs array detector cooled to -90 °C. The driving injection current is in the range of 1.25−1250 mA/cm2. The obtained EL spectra intensity was calibrated with the spectrum from a calibrated halogen lamp. The excitation wavelength for the PL was 470nm, and we kept the cell under open circuit and adjusted the laser intensity to reach open circuit condition similar to 1 sun.

External quantum efficiency (EQE). The measurement was measured using a grating spectrometer (CS260-RG-4-MT-D) to create monochromatic light combined with a tungsten halogen light source. The monochromatic light was chopped at ~300 Hz, and a Stanford Research Systems SR380 lock-in amplifier with an internal transimpedance amplifier of 106 V/A was used to detect the photocurrent. Long pass filters at 610, 715, 780, 850, and 1000 nm were used to filter out the scattered light from the monochromator. The spectra were taken from 300 to 1300 nm and calibrated by a silicon photodiode and a calibrated germanium photodiode.

JV characterization was carried out on 9 different cells for each Sn concentration, while all the other opto-electronic (JVT, CfT, CV, EL, PL and EQE) measurements were carried out on the single best representative among those 9.

XRF AND XRD OF THE DIFFERENT ABSORBERS

Table S1: metal ratios measured with XRF(X-ray fluorescence**) of selenized absorber for increasing nominal Sn content in the precursor solution expressed in atomic percentage.**

	Cu/Zn	Cu/Sn	Cu/Zn+Sn	Zn/Sn
A – 27.6 at.%	1.37	1.90	0.80	1.39
B – 29.5 at.%	1.41	1.88	0.80	1.34
C – 31.2 at.%	1.35	1.75	0.76	1.30
D – 32.9 at.%	1.37	1.64	0.74	1.20
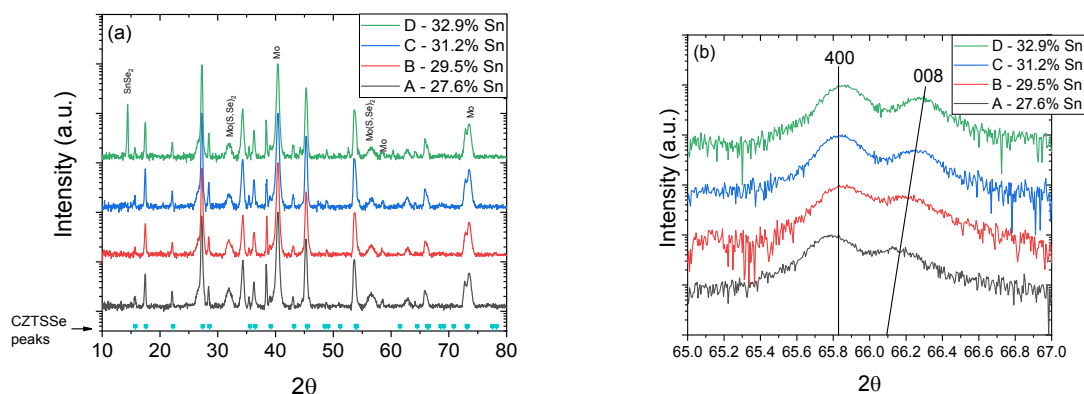
Figure S1: XRD pattern from 10 to 80° for all the devices a). High resolution XRD pattern from 65 to 67° after stripping Kα2 signal b).

X-ray diffraction patterns (10° < 2θ < 80°) shown in Figure S2a confirm unambiguously the CZTSSe phase with Bragg reflexes at 17.44°, 27.25° and 45.32°. For the device D the secondary phase $Sn(S,Se)_2$ can be identified with the peak at 14.42°,[1] which agrees with previous results shown in literature with Sn variation in the composition of the absorber.[2]

In figure S1b XRD scans of the 400-008 Bragg peaks reveal a shift of the 008 Bragg reflex toward bigger angles with increasing Sn content. This shift correlates with decrease in lattice parameter *c*, which signifies a decreased disorder of the Cu/Zn sublattice.[3] This supports the hypothesis according to which an increase in Sn content relates to the formation of Cu-poor kesterite. [2]
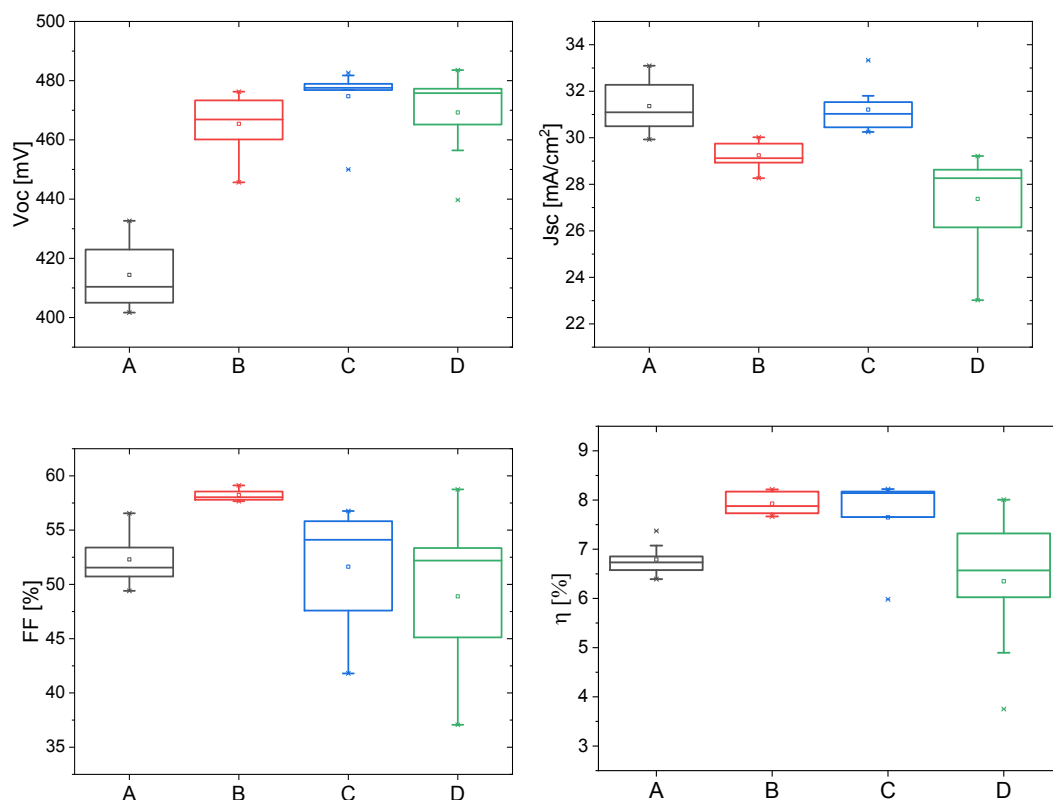
DEVICE PERFOMANCE DATA

Figure S2: Photovoltaic performance parameters as a function of Sn content measured with ARC (Anti-reflection coating). Each box plot represents 9 cells with an area of 0.3 ± 0.02 cm².

The increase in Sn content up to 31.2 at.% (device C) shows a clear improvement in the V_{oc} parameter which is reflected in the efficiency (Figure S3d). The lower performance for device D is correlated with the presence of the $SnSe_2$ secondary phase.
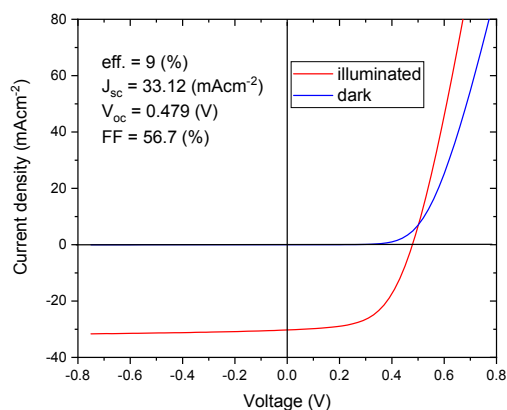

Figure S3: dark and illuminated JV for champion device with a Sn content of 31.2 at.% (device C).

Figure S4 shows illuminated and dark IV measurements for the champion device (device C) and a band gap of 1.14 eV as obtained from the inflection point of the first derivative of EQE curve. The V_{oc} deficit amounts to $\frac{E_g}{q} - V_{oc} = 0.66$ V. The power conversion efficiency of 9% with anti-reflective coating was determined for designated illumination area of 0.274±0.003 cm² including front contact metal grid.
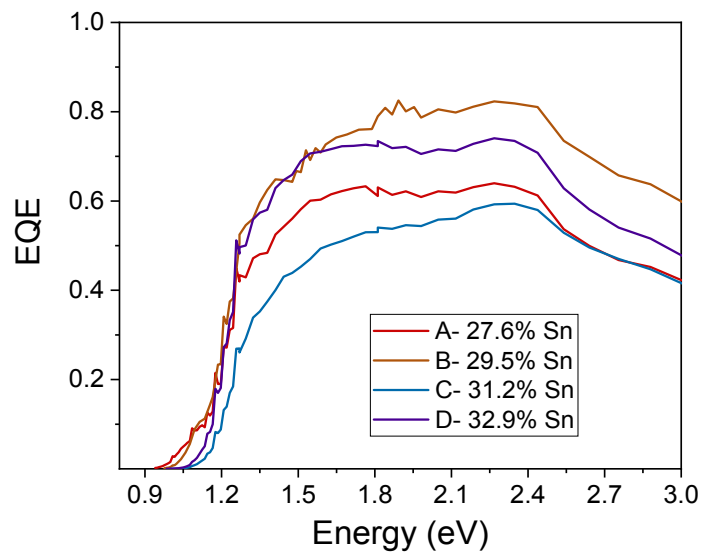
EQE SPECTRA

Figure S4 Measured EQE spectra for the 4 different cells.
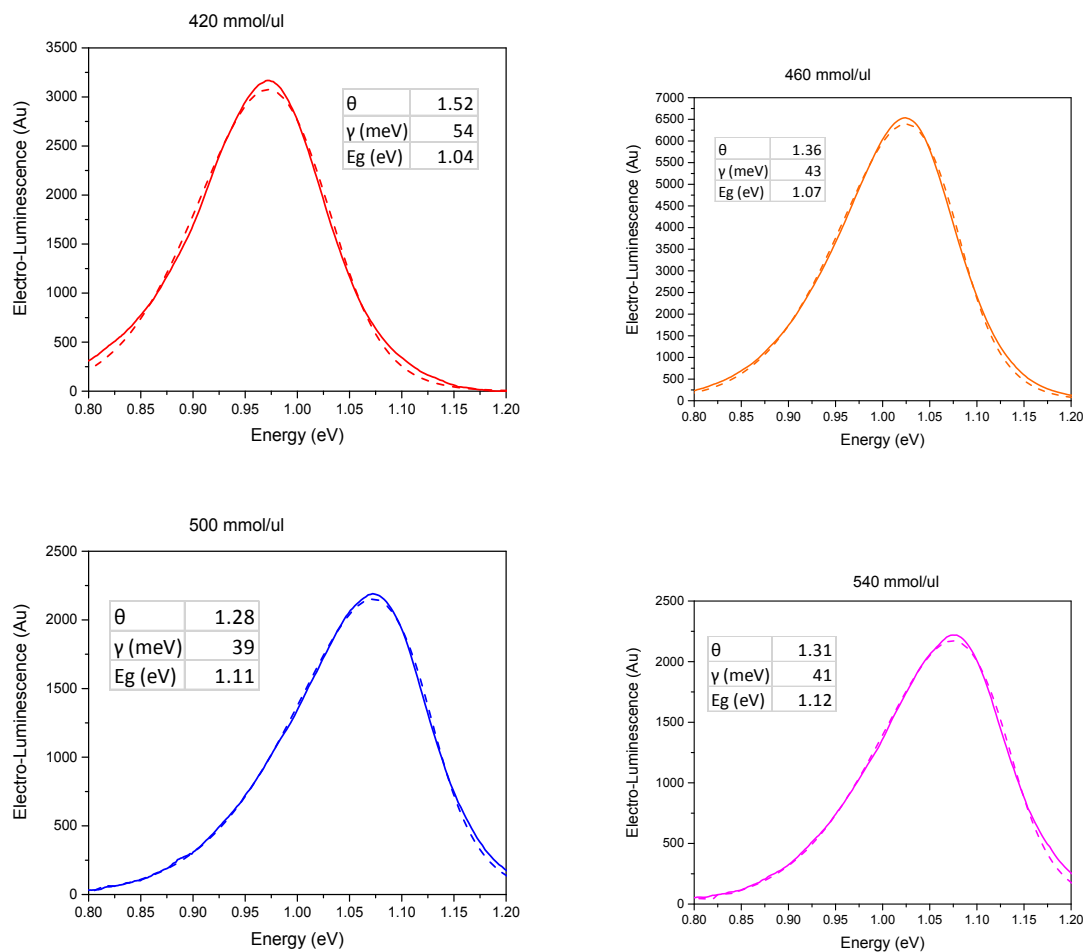
ELECTROLUMINECENCE SPECTRA FITTING PROCEDURE

Figure S5 Electroluminescence spectra of the four device types used to determine the band gap, along with the fit used to extract the band gap value.

We fit the electroluminescence of the cells using a model for the sub band gap absorption presented by Katahara et al.[4]. By convoluting a tail model and an ideal square root dependence above the band gap, the absorption coefficient can be expressed as :

$$\alpha(E) = \alpha_0(E) * \int_{-\infty}^{+\infty} \left(\exp\left(-\left|\frac{u}{\gamma}\right|^{\theta} \right) \sqrt{(E - E_g) - u} \, du \right.$$

Where the exponent θ may vary from 0.5 to 2, reflective of the Halperin & Lax and Sayakanit treatments.[5] The energy γ account for the different process causing a non ideal behaviour of the tail states density: Urbach (for $\theta = 1$), screened Tomas Fermi ($\theta = 1.25$), Franz-Keldysh ($\theta = 1.5$) Thomas-Fermi splitting ($\theta = 2$). The luminescence spectrum is estimated using 'Lasher-Stern-Wurfel' equation:

$$I_{EL}(E) = N * E^2 * \frac{1 - \exp(-\alpha(E)d)}{\exp\left(\frac{E - \Delta\mu}{kT}\right) - 1}$$

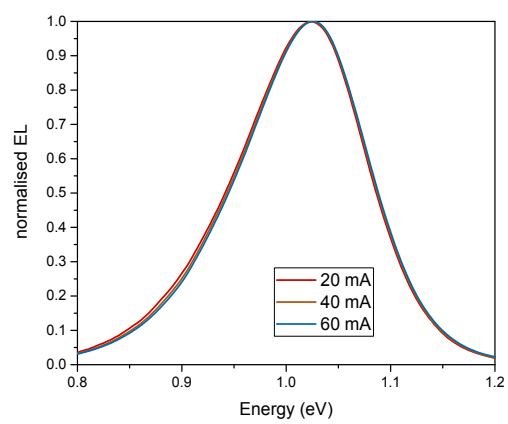Where $\Delta\mu$ is the quasi Fermi level splitting and N a normalisation factor.

Figure S 6 Electroluminescence spectrum of device B at three different injection currents from 20 mA to 60 mA.

COMPLEMENTARY VOLTAGE LOSSES ANALYSIS

Table S2: Summary of the voltage losses analysis for the four cells analysed with different Sn content, E_g are in eV, the voltages are in mV. $E_{g,EQE}$ and $E_{g,EL}$ refer to the band gap extracted from the EQE spectra and from the EL spectra respectively. $V_{oc,deficit,EQE}$ and $V_{oc,deficit,EQE}$ refer to the differences $E_{g,EQE}/q - V_{oc}$ and $E_{g,EQE}/q - V_{oc}$, respectively, where q is the electronic charge.

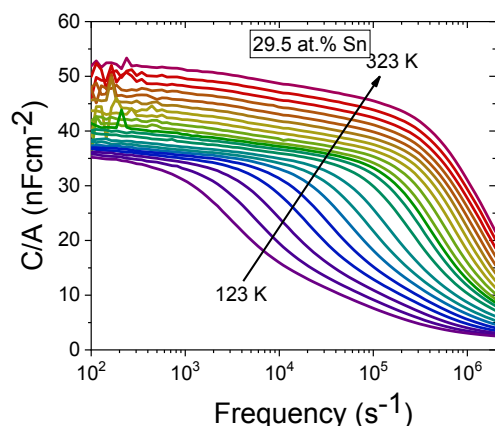| Label	Sn content	$E_{g_{EQE}}$	$E_{g_{EL}}$	V_{oc}	$V_{oc,deficit,EQE}$	$V_{oc,deficit,EL}$
A	27.6%	1.13	1.04	423	707	617
B	29.5%	1.14	1.07	453	687	617
C	31.2%	1.14	1.11	485	655	625
D	32.9%	1.15	1.12	465	685	655

Table S3: Summary of the voltage losses analysis for the four cells with different Sn content, E_g are in eV, the voltages are in mV. $V_{oc,SQ,EQE}$ and $V_{oc,SQ,EL}$ refer to the Shockley-Queisser open-circuit voltage limit corresponding to the bandgap extracted from the EQE spectra and from the EL spectra, respectively. Similarly, $V_{oc,abs,EQE}$ and $V_{oc,abs,EL}$ refer to the loss in Voc due to the non-sharp absorption edge for the two respective ways of determining band gap. $V_{oc,rad}$ is the radiative open-circuit voltage limit. Note that this quantity does not depend on the value of the band gap.

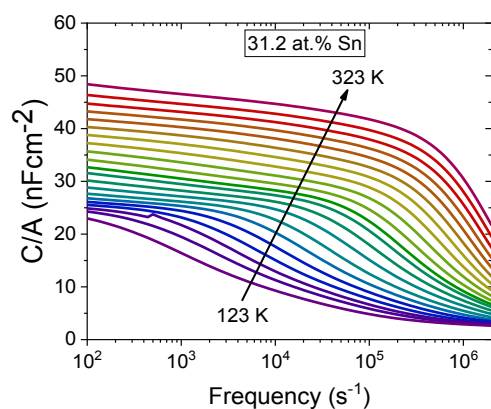| Label	Sn content	$E_{g_{EQE}}$	$V_{oc,SQ,EQE}$	$E_{g_{EL}}$	$V_{oc,SQ,EL}$	$V_{oc,rad}$	$\Delta V_{oc,abs,EQE}$	$\Delta V_{oc,abs,EL}$
A	27.6%	1.13	877	1.04	800	799	78	1
B	29.5%	1.14	887	1.07	828	840	47	-12
C	31.2%	1.14	887	1.11	866	888	-1	-22
D	32.9%	1.15	896	1.12	875	904	-8	-29

Focussing on the devices with the highest and lowest Sn contents (devices A and D, respectively), we first note that the $V_{oc,SQ}$ calculated from $E_{g,EL}$ is similar to $V_{oc,rad}$ for device A whereas it is higher by 30 mV for device D (Table S3). Secondly, we note that $V_{oc,SQ}$ calculated from $E_{g,EQE}$ is higher than $V_{oc,rad}$ for device A by 78 mV, and similar to $V_{oc,rad}$ for device D (Table S3)

TEMPERATURE DEPENDENT CAPACITANCE-FREQUENCY (CF-T) PLOTS FOR THE REMAINING DEVICES
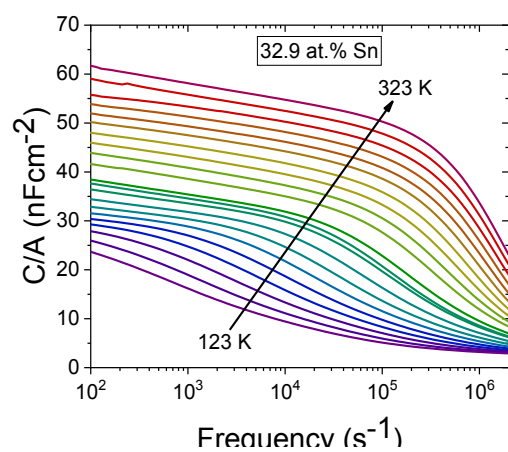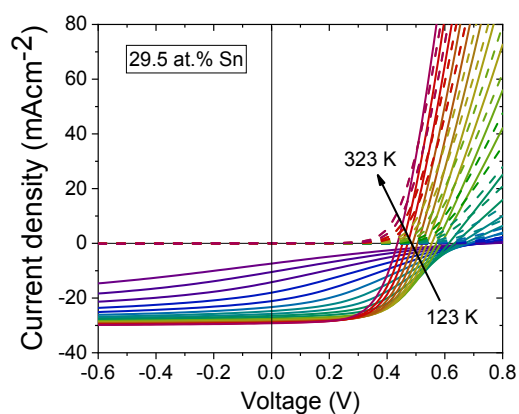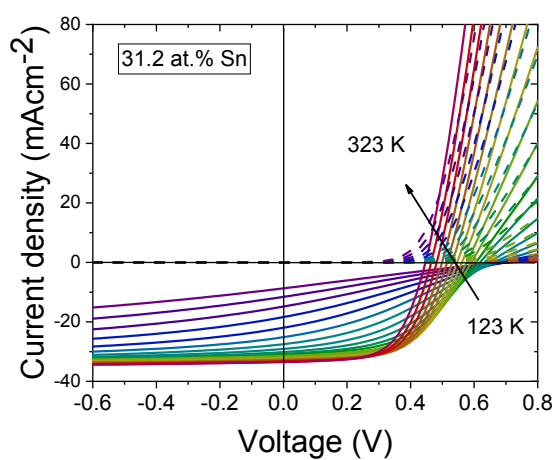
Device B:

Device C:

Device D:

TEMPERATURE-DEPENDENT CURRENT DENSITY-VOLTAGE PLOTS FOR THE REMAINING DEVICES.
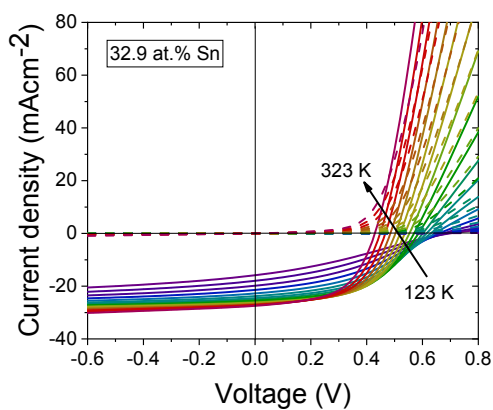
Device B:

Device C:

Device D:

Figure S8: temperature-dependent J-V measurement (dark curve: dotted line, light curve: solid line) of devices B, C and D (Sn content of 29.5%, 31.2% and 32.9% respectively). The data for A are shown in the main text.

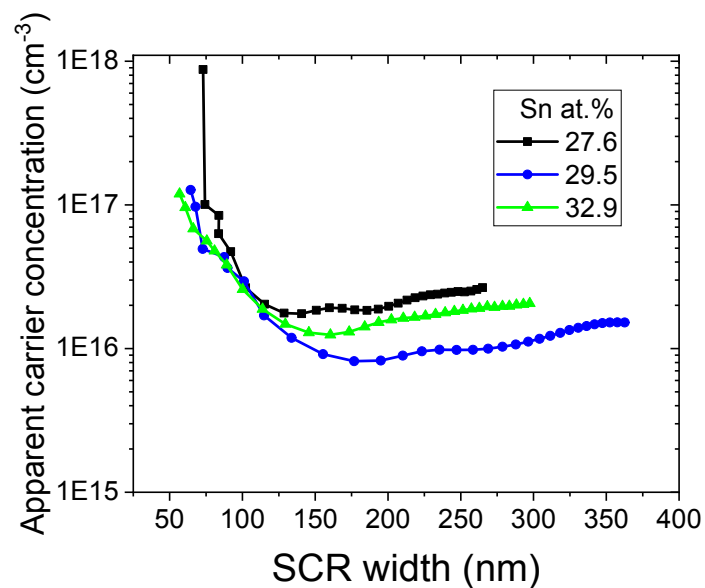## CAPACITANCE VOLTAGE MEASUREMENTS OF DIFFERENT DEVICES

Figure S9: Capacitance-voltage measurement of devices A, C and D (Sn content of 27.6%, 31.2% and 32.9% respectively) with voltage sweeping from -1 V to 0.5V at room temperature.
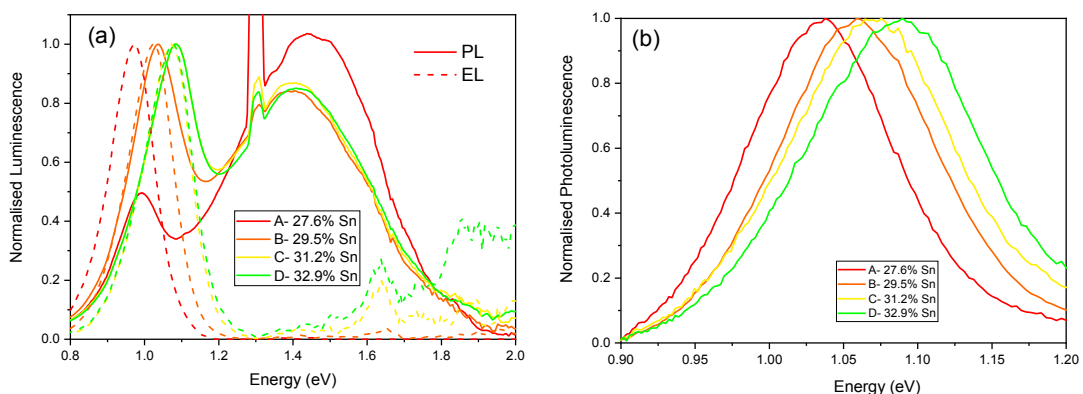
FULL PL SPECTRA

Figure S10 : (a) Full El and PL spectra of the figure shown in the main text figure 1, the PL was measured at ICL with an excitation wavelength of 470nm and under open circuit condition (light intensity adapted for a V_{oc} approaching V_{oc} under 1 sun). (b) PL measurements at EMPA with an excitation wavelength of 639nm and continuous wave excitation.

The presence of a second peak in the PL of figure S10a is unusual and as for now not fully understood, it was observed under different light intensities and on different samples. However, the measured EL did not show the second peak. Same applies for PL measurements made at EMPA (figure S10b) under different conditions.

REFERENCES

(1)   Liu, K.; Liu, H.; Wang, J.; Feng, L. Synthesis and Characterization of SnSe2 Hexagonal Nanoflakes. *Mater. Lett.* **2009**, *63* (5), 512–514. https://doi.org/10.1016/j.matlet.2008.10.054.

(2)   Haass, S. G.; Andres, C.; Figi, R.; Schreiner, C.; Bürki, M.; Romanyuk, Y. E.; Tiwari, A. N. Complex Interplay between Absorber Composition and Alkali Doping in High-Efficiency Kesterite Solar Cells. *Adv. Energy Mater.* **2017**, *8*, 1701760. https://doi.org/10.1002/aenm.201701760.

(3)   Márquez, J.; Neuschitzer, M.; Dimitrievska, M.; Gunder, R.; Haass, S.; Werner, M.; Romanyuk, Y. E.; Schorr, S.; Pearsall, N. M.; Forbes, I. Systematic Compositional Changes and Their Influence on Lattice and Optoelectronic Properties of Cu2ZnSnSe4kesterite Solar Cells. *Sol. Energy Mater. Sol. Cells* **2016**, *144*, 579–585. https://doi.org/10.1016/j.solmat.2015.10.004.

(4)   Katahara, J. K.; Hillhouse, H. W. Quasi-Fermi Level Splitting and Sub-Bandgap Absorptivity from Semiconductor Photoluminescence. *J. Appl. Phys.* **2014**, *116* (17). https://doi.org/10.1063/1.4898346.

(5)   Halperin, B. I.; Lax, M. Impurity-Band Tails in the High-Density Limit. I. Minimum Counting Methods. *Phys. Rev.* **1966**, *148* (2), 722–740. https://doi.org/10.1103/PhysRev.148.722.